MATERIALS SCIENCE

Time-resolved atomic-resolution Brownian tomography of single nanocrystals reveals size-dependent dynamics

Rubén Meana-Pañeda[1], Canran Ji[1,2], Cong T. S. Van[1], Cyril F. Reboul[1], Sungsu Kang[3], Sungin Kim[4], Jinho Rhee[5,6], Yunseo Lee[5,6], Peter Ercius[7], Wojciech Czaja[2], Jungwon Park[5,6,8,9]*, Hans Elmlund[1]*

Atomic-resolution structure identification of nanocrystals by graphene liquid cell electron microscopy (GLC-EM) has revealed that small, solubilized platinum nanocrystals consist of an ordered crystalline core surrounded by mobile surface atoms, which dissociate during oxidative etching, resulting in distinct temporal structural states. Requirements imposed by the 3D reconstruction algorithm limit the number of structural states that can be resolved. We introduce a regularized 3D reconstruction algorithm that exploits the redundancy inherent in the experimental data, allowing us to improve the time resolution. Our developments provide a comprehensive molecular picture at unprecedented spatial and temporal resolution of the nonlinear, linear, and fluctuating dynamic phenomena that single nanocrystals undergo during the GLC-EM experiment. We determined atomic structures of 66 temporal structural states, extracted from 15 time trajectories of individual nanocrystals. Large (478 to 698 atoms) and small (<300 atoms) nanocrystals show etching that preserves a stable core, whereas mid-sized (351 to 571 atoms) nanocrystals present dynamics that change the coordination of the core.

INTRODUCTION

The field of nanoscience largely lacks methods to probe nonequilibrium species in nanomaterials, with a few notable exceptions (*1*, *2*), and robust methods for three-dimensional (3D) structure determination of nanocrystals in solution have proven extremely difficult to develop. Presynthesized nanocrystals are susceptible to subsequent rearrangements in solution through surface atom desorption and adsorption, coalescence, and dissolution following Ostwald ripening (*3*, *4*). 3D structure determination of single nanocrystals in solution by graphene liquid cell electron microscopy (GLC-EM) and single-particle analysis (*2*, *5*–*7*) may provide answers to long-sought physical models for nanocrystal formation, growth, and dissolution. However, several fundamental limitations need to be overcome before the method can become a robust route to probing nonequilibrium nanocrystal species. This study represents a major step in this direction.

In biological single-particle cryo–electron microscopy (*8*), experimental measurements are abundant, and the main challenges are the extreme levels of noise (*9*) and the molecular heterogeneity of the single-particle ensemble (*10*). In contrast, transmission electron microscopy (TEM) images of metallic nanoparticles have higher signal-to-noise ratio (SNR) because the difference in phase contrast between the light atom background (graphene and water) and the heavy metallic atoms is relatively large. However, we are imaging nanocrystals undergoing time-dependent structural changes of unknown nature at unknown timescales. Direct electron detectors available for in-solution experiments can be used to acquire a few tens of thousands of single-nanoparticle 2D views in different 3D orientations, obtained over a few tens of seconds at high electron dose. Unless the rotational freedom of the nanocrystal is completely unrestricted, which is rarely the case, we are faced with the problem of trying to obtain atomic-resolution 3D movies of dynamic structural phenomena from a set of differently projected 2D views of a nanocrystal with limited rotational sampling. This problem requires sophisticated methods for signal enhancement that go beyond straightforward averaging.

Biological single-particle EM favors computational approaches that can estimate accurate relative 3D particle orientations, on average, in a computationally efficient manner (*11*–*14*), whereas 3D reconstruction of metallic nanoparticles from GLC-EM images requires very accurate and precise determination of each of the relative 3D orientations because of the scarcity of recorded particle views. In biological single-particle EM, prohibitively large 3D reconstruction errors can be overcome by collecting more data, whereas this approach is infeasible for nanocrystals in solution. The evaporation under electron irradiation in ultrahigh vacuum causes rapid shrinkage of the cell to a degree that does not allow free nanocrystal rotation. Data are collected in Scherzer focus of an aberration corrected instrument (*15*). Hence, for all practical purposes, there is no contrast transfer function (CTF) (*16*) to account for. The model that we seek to estimate is typically well represented by a periodic arrangement of atoms, and sophisticated regularization approaches involving the CTF are not needed. Therefore, more directly applicable approaches for regularization compared to those used in biological single-particle EM can be pursued.

This study introduces three principal innovations to nanoparticle 3D reconstruction with GLC-EM to enable time-resolved quantitative 3D structure analysis at the highest possible temporal and spatial resolution. First, the atomic model building is coupled in an iterative manner to the method that we previously developed for estimating the relative 3D orientations (*5*–*7*). Second, denoising of the nanoparticle time trajectory through nonlinear dimensionality

[1]Center for Structural Biology, Center for Cancer Research, National Cancer Institute, Frederick, MD 21702, USA. [2]Department of Mathematics, University of Maryland, College Park, MD 20742-4015, USA. [3]Department of Chemistry, University of Chicago, Chicago, IL 60637, USA. [4]Department of Chemistry and Chemical Biology, Cornell University, Ithaca, NY, USA. [5]Center for Nanoparticle Research, Institute for Basic Science (IBS), Seoul 08826, Republic of Korea. [6]School of Chemical and Biological Engineering, Institute of Chemical Process, Seoul National University, Seoul 08826, Republic of Korea. [7]National Center for Electron Microscopy, Molecular Foundry, Lawrence Berkeley National Laboratory, Berkeley, CA 94720 USA. [8]Institute of Engineering Research, College of Engineering, Seoul National University, Seoul 08826, Republic of Korea. [9]Advanced Institute of Convergence Technology, Seoul National University, Suwon-si, Gyeonggi-do 16229, Republic of Korea.
*Corresponding author. Email: jungwonpark@snu.ac.kr (J.P.); hans.elmlund@nih.gov (H.E.)

reduction before 2D and 3D registration overcomes the need for anisotropic motion correction and averaging of contiguous movie frames in small time windows, as previously described (*7*). Third, to account for further variability within the discrete temporal state groups, for example, due to regional surface disorder, or partial occupancy of associating atoms, we introduce a method for adaptive nonuniform regularization based a spatially varying real-space prior that optimizes the atomicity of the reconstructed 3D density maps. With these methodological advancements, we could reliably reconstruct 66 atomic-resolution 3D density maps from 15 previously acquired nanocrystal time trajectories (*2*, *5*–*7*). In addition to allowing estimation of the rate of structural change, our analysis enabled estimation of time-dependent atomic lattice and shape properties. Below, we provide time-dependent statistics of various atomic lattice descriptors, such as coordination number (CN), radial strain, and crystallinity score. The ability to measure dynamic atomic parameters in space and time represents the next frontier of structural studies in solution.

RESULTS

Our previous developments for 3D reconstruction of nanocrystal time trajectories (*2*, *5*–*7*) suffered from issues with convergence stability and had to be repeated multiple times to ensure convergence to a global optimum. If the foreground atomic contrast managed to drive the 3D reconstruction process to early convergence, then interpretable atomic-resolution 3D reconstructions could be obtained. However, if background signal from the solvent and the graphene started biasing the 3D reconstruction, convergence stalled, and the maps became streaky and problematic with poorly defined atomicity. To overcome this problem, we here introduce a method that couples the iterative 3D refinement with unsupervised atomic model building and applies a spatially varying real-space prior that optimizes the atomicity of the reconstructed density maps (Materials and methods). Figure 1 provides a schematic overview of our method.

We reanalyzed seven time trajectories that we previously analyzed with earlier generations of our 3D reconstruction methodology, four from (*5*) (NP3, NP1, NP4, and NP5 in fig. S1A) and three from (*17*) (NP1, NP2, and NP7 in fig. S1B). In addition to the added value that the time-dependent structural information gives with our methodology, we also obtained substantially improved 3D reconstruction quality in five of the seven tests and maps of comparable quality in the remaining two tests, as measured by the average correlation between the experimentally reconstructed atomic densities and simulated atomic densities (*7*, *17*). NP3 from (*5*) showed an average improvement of 19.2% in atom correlation, and the closest matching temporal state differed in composition by 2.3% of the total mass. NP1 from (*5*) showed similar atom correlation of ~0.8 in the time-segmented

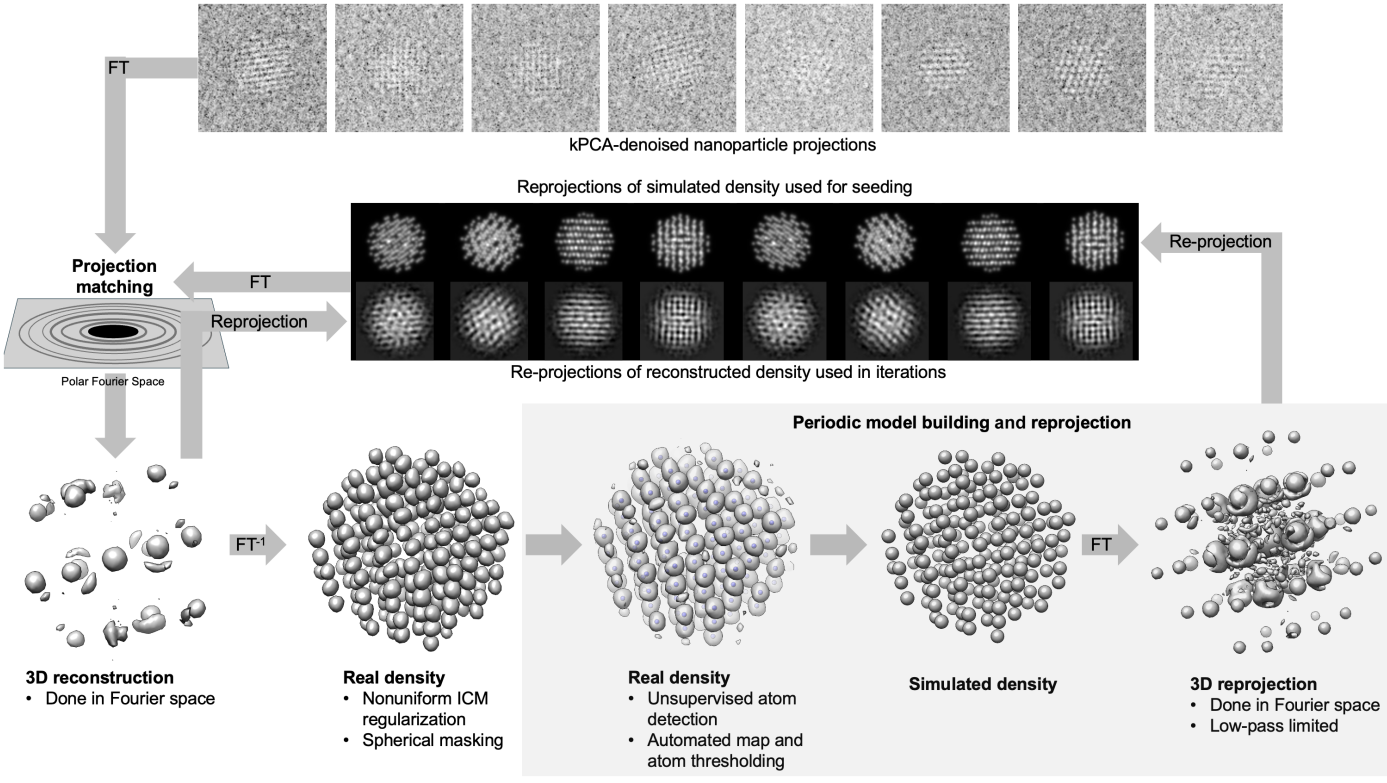

Fig. 1. Schematic summary of our method for regularized nanoparticle 3D reconstruction. Individual nanoparticle projections, denoised with kernel–principal components analysis (kPCA), are matched with reprojections of the 3D density map. Reprojections of the simulated density map are used for seeding the projection matching and reprojections of the reconstructed density are used in the iterations that follow. After one cycle of iterative 3D orientation refinement with projection matching is completed, atom segments and their center coordinates are identified in an unsupervised fashion using automated map and atom peak thresholding. A simulated density is produced from the atomic coordinates and used to reseed the next cycle of the process. The real density was rendered at slightly higher sigma value in the picture that demonstrates the unsupervised atom detection to include some nonatom noisy background signal and illustrate the power of the automated map/atom thresholding. ICM, iterated conditional mode; FT, Fourier transform.

maps versus the time-integrated map and a 3.9% difference in composition of the closest matching state. NP4 from (*5*) showed similar atom correlation of ~0.75 in the time-segmented maps versus the time-integrated map and but the difference a higher compositional difference (17.1%) of the closest matching temporal state. NP5 from (*5*) showed an average improvement of 10% in atom correlation and a compositional difference of 11.6% in the closest matching temporal state. NP1 from (*17*) showed an average improvement of 14.4% in atom correlation and a substantial difference in composition (19.2%) in the closest matching temporal state. NP2 from (*17*) showed an average improvement of 2.8% in atom correlation and difference in composition of 19.4% in the closest matching temporal state. NP7 from (*17*) showed an average improvement of 16.9% in atom correlation and difference in composition of 13.9% in the closest matching temporal state. Overall, the regularized 3D reconstruction approach identifies fewer atoms with improved atomicity overall. The most dramatic improvements are seen in NP3 and NP4 from (*5*) and in NP1 and NP7 from (*17*) In these instances, the surface structure is much better defined in the maps obtained with regularized time-resolved 3D reconstruction. The facets of the nanocrystal are resolved, which is a strong indication that alignment errors have been reduced, and compositional surface variations resolved.

Time-resolved atomic-resolution 3D reconstruction of 15 nanocrystal time trajectories

Trial time segment boundaries were identified on the basis of reprojection correlation plots (fig. S2), which plot the correlation between reprojections of the time-averaged 3D reconstruction and the individual nanocrystal views in the time trajectory as a function of time. Any major 3D structural differences between the time-averaged 3D reconstruction and the individual nanocrystal views will be reflected in the magnitude of the correlation. This resulted in an initial division of each trajectory into one to four contiguous time segments. Independent 3D reconstructions were obtained from these segments before conducting further splitting. Further splitting of the time trajectory was a process of trial and error, splitting further and further until reliable 3D reconstructions and associated atomic models could not be produced. Three to eight time-windowed atomic-resolution 3D reconstructions, ranging in time window size from 2.5 to 19.8 s, with an average segment size of 7.2 ± 4.0 s, were obtained per nanocrystal time trajectory. We selected the size of the time windows to allow successful atomic-resolution 3D reconstruction with sufficient rotational coverage, which does not necessarily reflect the physical lifetime of the reconstructed temporal states. However, we find it unlikely that there would be major structural transitions occurring within the individual segments analyzed because of the exceptionally high quality of the maps produced. In those instances where reliable atomic-resolution 3D reconstructions and associated atomic coordinates could be determined of highly similar structural states that were neighbors in time, we could ascertain the degree of structural stability with high confidence and compare atom association/dissociation rates between different time segments. It is also important to characterize strain, the relative deformation of the nanocrystal when compared to an ideal face-centered cubic (FCC) lattice. Strain is an important descriptor that accounts for the reactivity of Pt nanocrystals in important catalytic reactions, including the methanol oxidation reaction and the oxygen reduction reaction (*18*, *19*) as strain modifies the local binding energy of adsorbates by changing the bandwidth of the *d* orbitals (*20*). We obtained 3D strain maps for each temporal structural state, as described in Materials and Methods.

Findings for all trajectories are summarized in table S1. Definitions for the different categorizations used are summarized in table S2. We began analyzing the results for the smallest nanocrystal [trajectory ESC5 (etching with stable core 5); Fig. 2A]. This nanocrystal has 182 atoms in the initial temporal state and 163 atoms in the final state. It loses 10% of its total mass through etching while maintaining a stably coordinated core of atoms. The fraction of atoms with CN > 8 decreases linearly throughout the trajectory from 59 to 53%. We previously reported that crystal abnormalities resulting from surface interactions with ligands, the solvent, and the electron beam have a "penetration depth" δ beyond which the nanocrystal approximates an ideal FCC lattice (*17*). It is at this depth that a transition occurs within the nanocrystal itself from a lowly coordinated irregular surface to a highly coordinated core. An increase in penetration depth with time would indicate an increase in surface disorder and irregularity, whereas a decrease in penetration depth means that a larger fraction of the total number of atoms of the nanocrystal is part of the highly coordinated core. The penetration depth only shows minor variations over the ESC5 trajectory, with an overall increase of 0.32 Å (~8% of the lattice parameter of bulk Platinum). ESC5 has one of the most stable structures observed in this study.

Next, we turned to trajectory FCHCS1 (fluctuating atom composition, high core stability 1; Fig. 2B), showing a nanocrystal with fluctuating atomic composition and high core stability. The first three time-segments, spanning the first 10 s, show nearly identical structures, indicating a high degree of stability. The change in penetration depth and degree of coordination in the first 10 s are minor, whereas the average radial strain peaks at 23 s, right before the loss of 13% of the total mass of the particle in the last transition, and reversion back into a final temporal state with nearly identical composition compared to the initial three states. The end state has the largest penetration depth and the least coordinated core of the four FCHCS1 time segment structures.

Trajectory ESIP1 (etching with stable initial phase 1; Fig. 2C) displays an equally high degree of stability, with three identical time segment 3D reconstructions spanning the first 15 s, followed by a rapid dissolution event (−8.3 atoms/s). The penetration depth remains unchanged with time, and the particle only loses 13% of its total mass during imaging. This high degree of structural stability is the hallmark of small (163 to 285 atoms) nanocrystals.

Next, we turned to trajectory EFC4 (etching with fluctuating core 4; Fig. 2D), which represents a nanocrystal of 316 atoms that undergoes etching with fluctuating core to lose 30% of its total mass. This is the first example of a nanocrystal with a core fluctuating between 60 and 64% of atoms with CN > 8 across the trajectory. The penetration depth is also fluctuating with time, indicating that when nanocrystals have reached this size, there is a correlation between dynamic effects at the surface and the stability of the core.

Trajectory EFC2 (Fig. 2E) also undergoes etching with a fluctuating core, but this nanocrystal of 337 atoms displays a much more dramatic dissolution trajectory with a highly nonlinear overall etching process proceeding over three structurally stable phases. The penetration depth peaks at 20 s, which is the point at which the core is the least coordinated. Hence, the reconstruction at 20 s likely represents a transient intermediate in the dissolution trajectory. The average radial strain accumulates throughout the trajectory and reaches its peak after 36 s. The structure with the highest stability

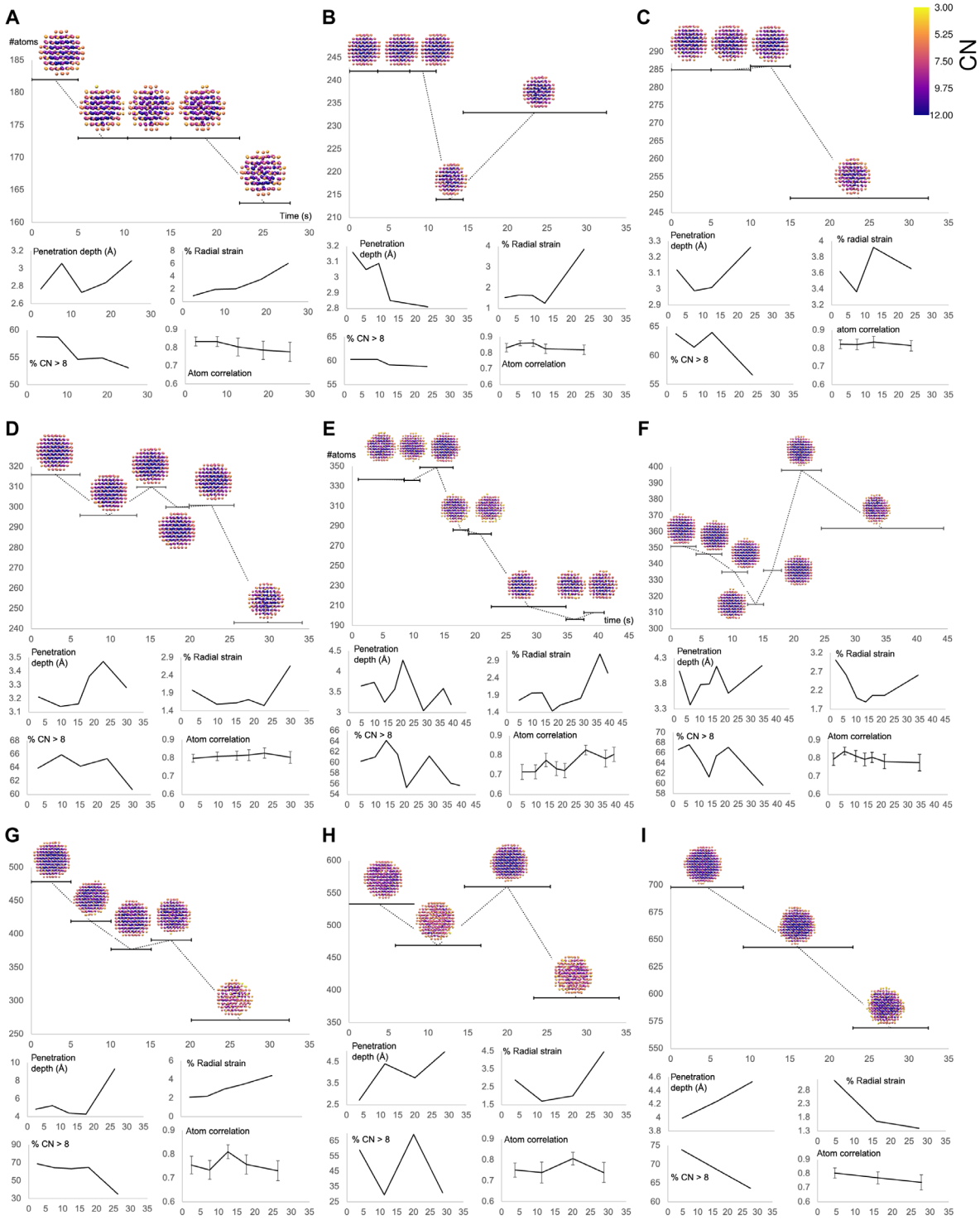

Fig. 2. Evolution of the nanocrystal structures as a function of time. The individual atoms are color-coded according to CN. The four plots below the trajectory of 3D atomic coordinates show as a function time: the penetration depth, the average radial strain, the fraction of atoms with CN > 8, and the average and SD of the correlation between the individual atomic densities and the density of a simulated atom, as described in the main text. (**A**) ESC5 trajectory, an example of etching with stable core. (**B**) FCHCS1 trajectory, an example of fluctuating composition with high core stability. (**C**) ESIP1 trajectory, an example of etching with stable initial phase. (**D**) EFC4 trajectory, an example of etching with fluctuating core. (**E**) EFC2 trajectory, an example of etching with fluctuating core. (**F**) FC1 trajectory, an example of fluctuating atom composition. (**G**) ESC3 trajectory, an example of etching with stable core. (**H**) EFC1 trajectory, an example of etching with fluctuating core. (**I**) ESC1 trajectory, an example of etching with stable core.

appears in the end of the EFC2 trajectory, with three remarkably similar temporal states of 209, 196, and 203 atoms, respectively, extracted from the last ~20 s of the ~40-s-long trajectory. The last of the three temporal states in the first structurally stable phase of the EFC2 trajectory shows a peak in core coordination at 15 s. The first temporal state in the third and last structurally stable phase of the EFC2 trajectory, right after the second major transition, show a second peak in core coordination at ~30 s.

The FC1 trajectory (fluctuating core 1; Fig. 2F) undergoes dynamics leading to a small amount of growth (3% of the total mass). In the first 15 s of the FC1 trajectory, the nanocrystal undergoes highly linear etching, losing 10% of its total mass. During this phase, the fraction of atoms with CN > 8 is reduced from 67 to 61%. The nanocrystal then undergoes rapid growth with a growth rate of 13.2 atoms/s between the fifth and the sixth time segment. The final etching phase takes the nanocrystal from 398 to 362 atoms with a concomitant increase in strain and penetration depth.

Next, we analyzed the ESC3 trajectory (Fig. 2G). This larger nanocrystal of 478 atoms loses 43% of its mass through etching while preserving a stable core. The ESC3 dissolution dynamics is highly linear, and there is a large increase in penetration depth toward the end of the trajectory (after 20 s) concomitant with a drop in the fraction of highly coordinated atoms. The average radial strain increases linearly with time, inversely proportional to the degree of core coordination. However, linear dynamics are not the norm for larger nanocrystals, as demonstrated by trajectory EFC1 (Fig. 2H) showing a nanocrystal of 533 atoms undergoing etching with a fluctuating core to arrive at a state of 388 atoms, having lost 27% of its total mass. The % CN > 8 plot shows a sawtooth wave for this nanocrystal, which fluctuates markedly, going from 59 to 29% CN > 8 atoms in the first transition and from 69 to 31% CN > 8 atoms in the last transition. The 69% CN > 8 atoms is in the top three highest reported values in this study, but this highly crystalline state lasts for only 10 s before etching reduces its mass by 31% in a transition with the highest rate of change—20 atoms/s—measured in this study. The rate of change could be much faster because we presently do not have sufficient temporal resolution to assess exactly where the transition occurs, but it is not slower than reported.

Last, we report our findings on the largest nanocrystal analyzed (Fig. 2I). The ESC1 trajectory undergoes etching with a stable core with an initial state of 698 atoms and a final state of 569 atoms, thus losing 18% of its total mass. The dissolution dynamics are highly linear for this nanocrystal. All the extracted statistics show strongly linear dependency on time. The penetration depth increases linearly as the surface structure becomes less coordinated and more irregular, the radial strain decreases close to linearly, and the fraction of highly coordinated atoms decreases linearly with time.

An additional six trajectories are presented in fig. S3. All analyzed trajectories have high time-dependent atom correlations, indicating high 3D reconstruction quality and absence of any 3D reconstruction outliers due to, for example, limited sampling of projection directions.

Our detailed analysis enabled categorization of the type of dynamics observed for nanocrystals of different sizes (Table 1). In summary, the first category of dynamics we observe is etching that preserves a stable core throughout the entirety of the time trajectory or a substantial part of it. This category contains the largest nanocrystals (478 to 698 atoms) and the nanocrystals below 300 atoms in size. The second category of dynamics observed is etching that involves structural intermediates with a destabilized core structure, either a single destabilized intermediate state (nanocrystals in the size range of 353 to 571 atoms) or nanocrystals showing fluctuating core coordination (size range of 351 to 533 atoms). It is remarkable that the nanocrystals with the most stable core and the least relative change in mass are the two smallest nanocrystals with initial states of 242 and 182 atoms, respectively. In contrast, nanocrystals in the size range of 300 to 600 atoms show the largest relative change in mass and the largest change in the fraction of highly coordinated atoms with time. Therefore, we conclude that there is a strong size dependency on the stability of the nanocrystals, where below a certain threshold in size, the stability increases. It is also evident that highly nonlinear dynamic phenomena, such as fluctuating core coordination and fluctuating penetration depth predominantly, occur in mid-sized nanocrystals of 316 to 533 atoms. In contrast, larger nanocrystals of 520 to 698 atoms show linear dissolution dynamics and linear increase in penetration depth with time.

We next calculated the radial strain for each set of atomic coordinates (Materials and methods). Furthermore, to assess whether there existed a subset of atoms that remain in similar positions throughout the trajectory, we developed a method to identify the "time-invariant core" of atoms (Materials and methods). Last, we developed a scalar metric to assess the degree of crystallinity of a nanoparticle that does not make any assumptions about the fit of an ideal FCC lattice to the experimentally measured lattice geometry. This "crystallinity score" represents the probability that a nanocrystal atomic structure has an ideal FCC lattice geometry (Materials and methods). These results are presented for a subset of trajectories with noteworthy strain and core dynamics in Fig. 3. The ESC5 trajectory showed a linear increase in average radial strain (Fig. 1A), indicating an expansion of the lattice. At the atomic level, we detected a strain polarity at 13 s (Fig. 3A). The time evolution of the radial strain is not homogeneous across the atoms of the ESC5 trajectory. On average, there is a positive increase in strain, but a handful of atoms at the surface and in the center show negative strain.

Table 1. Type of dynamics observed for nanocrystals of different sizes.

182–285 atoms	316–353 atoms	478–698 atoms
ESC	EFC	ESC
Fluctuating atom composition, high core stability (FACHC)	Fluctuating atom composition (FAC)	EFC
Etching with stable initial phase (ESIP)	ECT	ECT

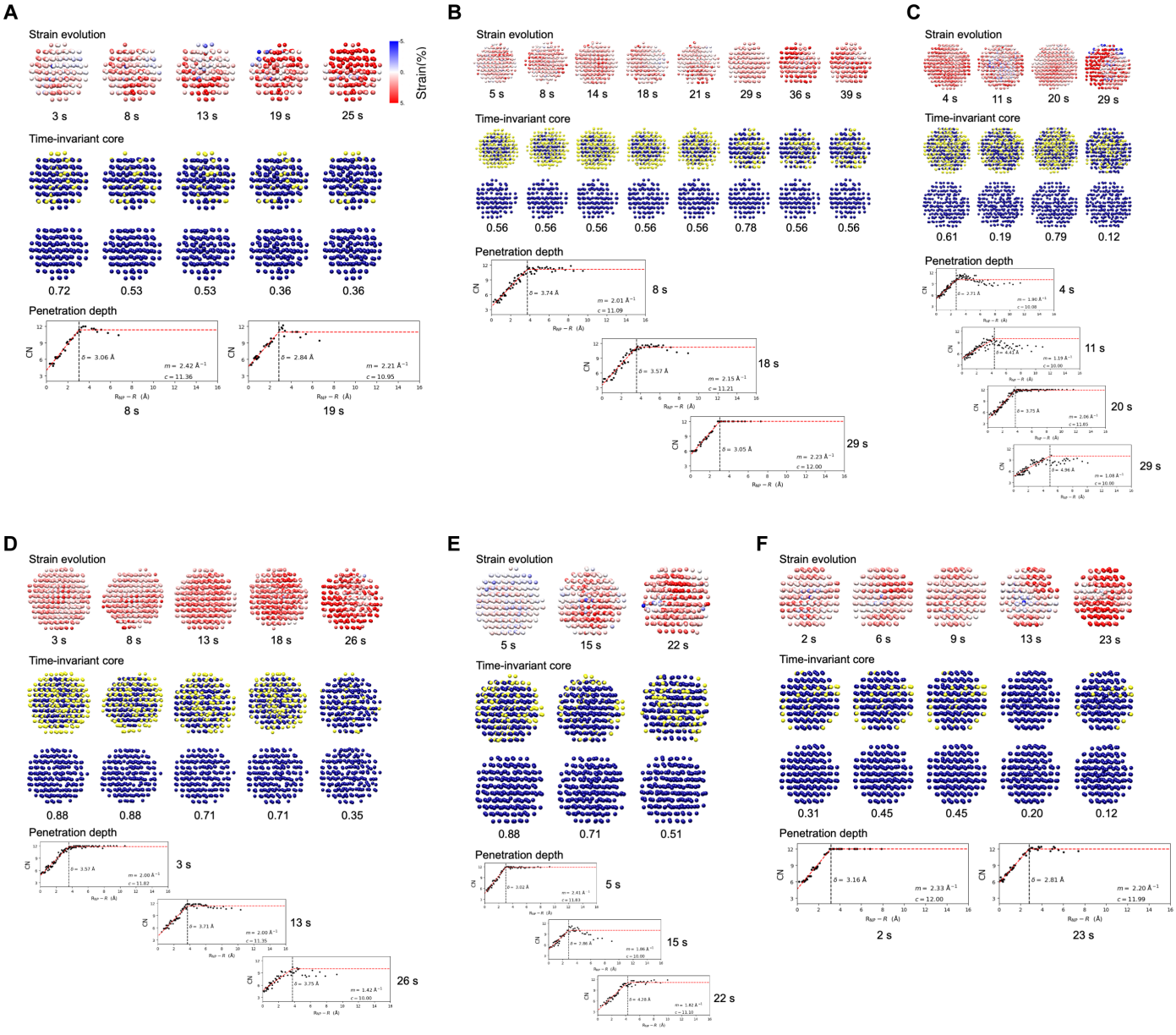

Fig. 3. Quantitative time-dependent structure analysis. The top panels show evolution of radial strain at the atomic level (blue to red atom coloring), the middle panels visualize the "time-invariant core" atoms (blue) and changing fringe atoms (yellow), and the lower panels show penetration depth plots for selected time segments. The timestamp (in s) is indicated below the atomic structures showing the magnitude of the radial strain, and the crystallinity score is indicated below the time-invariant core pictures (blue atoms). (**A**) ESC5 trajectory, an example of etching with stable core. (**B**) EFC2 trajectory, an example of etching with fluctuating core. (**C**) EFC1 trajectory, an example of etching with fluctuating core. (**D**) ESC3 trajectory, an example of etching with stable core. (**E**) ECT2 trajectory, an example of etching with core transition. (**F**) FCHCS1 trajectory, an example of fluctuating composition with high core stability.

The analysis of the time-invariant core of ECS5 shows a linear decrease in crystallinity score over time and most of the fringe atoms are confined to the surface. The penetration depth plots at 8 s versus 19 s indicate a slight drop in core coordination with time, but no notable change in penetration depth.

The EFC2 trajectory shows little change in average radial strain in the first 30 s, followed by a rapid increase (Fig. 1E). At the atomic level, all strain is either positive or close to zero (Fig. 3B). The pattern of change in strain magnitude with time indicates a bipartite division of atoms with either strain close to zero or atoms with positive strain, but the pattern varies in geometry across the trajectory. The analysis of the time-invariant core of EFC2 indicates a classic etching pattern with lowly coordinated surface atoms dissociating. Notably, the crystallinity score of the time-invariant core peaks at 29 s, right after the major structural transition in the dissolution trajectory. The penetration depth plots confirm that there is a disorder to order transition somewhere between 21 and 29 s.

The EFC1 trajectory shows an initial drop in average radial strain followed by a rapid increase toward the end of the trajectory (Fig. 1H). At the atomic level, the strain pattern is complex, with high positive

strain in the initial and final structures and a relaxed state at 20 s (Fig. 3C). This relaxed state shows the highest crystallinity score of the time-invariant core, and the penetration depth plots confirm the disorder to order transition.

The ESC3, ECT2 (etching with core transition 2), and FCHCS1 trajectories (Fig. 3, D to F) show unremarkable time-dependent dynamic changes compared to the above-described trajectories. The ESC3 trajectory shows linear increase in the average radial strain and the highest crystallinity score for the time-invariant core in the first 10 s (Fig. 3D).

The ECT2 trajectory starts off in a highly relaxed state (first 20 s) and then undergoes a rapid increase in average radial strain (fig. S3D). The crystallinity score decreases linearly, and there is a slight drop in core coordination at 15 s, as confirmed by the penetration depth plots (Fig. 3E).

The FCHCS1 trajectory shows little change in the average radial strain in the first 10 s and then a strain polarity at 13 s with two clusters of atoms with highly positive strain confined to the surface appears before the positive strain transcends to the entire particle (Fig. 3F). The highest crystallinity score is observed in the first 10 s.

Last, we plotted the crystallinity score as a function of the number of atoms for all time segment structures (Fig. 4), which revealed three groups of nanocrystals with distinct characteristics. The grouping simultaneously considered the number of atoms, the nature of the dynamic changes, and the crystallinity score. Small nanocrystals (163 to 301 atoms) have crystallinity scores ranging from 0.12 to 0.83. Medium-sized nanocrystals (310 to 469 atoms) have scores ranging from 0.51 to 0.98, and large nanocrystals (475 to 698) have scores ranging from 0.61 to 0.99. Two outliers were identified of temporal states with 388 and 469 atoms, respectively. Both outlying states are part of the EFC1 trajectory at 29 and 11 s, respectively. We have no reason to believe that these states are artifacts due to limited projection direction sampling (fig. S2) or poor 3D reconstruction quality (Fig. 2H, see atom correlation plot).

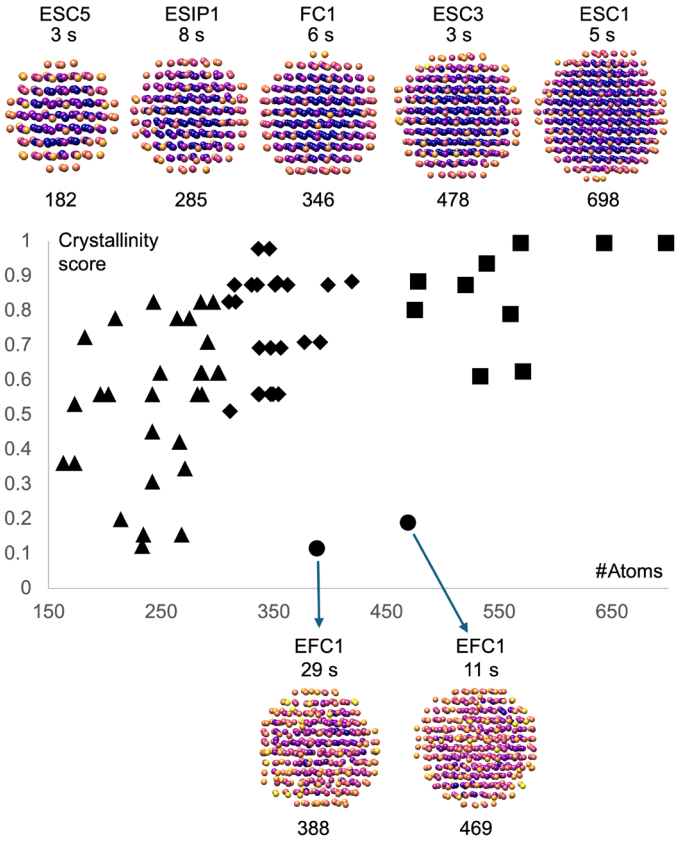

Fig. 4. Crystallinity score as a function of the number of atoms. The top panel show example structures with high crystallinity scores extracted from the indicated trajectories (top), with the number of atoms indicated (bottom). Triangles, diamond, and square markers correspond to the three categories of nanocrystals described in Table 1. The two indicated outliers correspond to the two structural intermediates in the EFC1 trajectory, with timestamps and number of atoms indicated.

DISCUSSION

We present 66 atomic structures of distinct temporal nanocrystal states, providing a plethora of information for theoreticians pursuing simulations of these types of systems. The dynamic structural insights we have gained and the computational framework we introduce for quantitative structural analysis of heterogeneous nanoparticles in solution will be valuable in research fields concerned with optimal material design in the many different areas where platinum nanocrystals have applications (*21*–*25*).

A subset of nanocrystals remains stable in certain time segments and then undergoes rapid and profound structural rearrangements. Referring to these dissolution dynamics as etching is appropriate because atoms are removed from the surface when we look at the start and the end structures. However, given the highly nonlinear changes in the number of atoms, the mechanism is different from that expected from classic equilibrium physics. Whether the dynamic surface effects we observe have direct mechanistic relevance to heterogeneous catalysis or are a consequence of interactions with the electron beam cannot be determined. It is likely that radiation damage of the organic ligands that cover the nanocrystal surface occurs already at a very low electron dose (5 to 10 e−/Å^2), as for proteins, and that we are in fact imaging nanocrystals with a damaged passivation layer. Improved data acquisition schemes, possibly under cryogenic conditions, applied to the appropriate nanocrystal systems in conjunction with robust quantitative image processing are needed in the future to further characterize these dynamic phenomena. However, it is evident that the methodology that we put forward for time-resolved Brownian tomography of single nanocrystals and regularized 3D reconstruction can be applied to characterize these kind of phase changes at the atomic level.

The trajectories that show the most complex nonlinear structural dynamics also show the most complex variations in penetration depth with time (Fig. 2, E and F), whereas trajectories that that display linear dissolution dynamics show linear change in penetration depth with time (Fig. 2I). The smallest structures (Fig. 2, A to C) show comparably small variations in penetration depth (ESC5, Fig. 2A: change of +0.3 Å in δ across the trajectory; FCHCS1, Fig. 2B: change of −0.35 Å; and ESIP1, Fig. 2C: change of +0.14 Å), whereas the penetration depth in the larger structures vary more (ESC1, Fig. 2I: change of +0.54 Å; ESC2, fig. S3E: change of +0.65 Å; and ESC3, Fig. 3G; change of +4.46 Å). As the number of atoms in a nanocrystal increases, the number of energetically accessible states also increases, as outlined by Bohr's correspondence principle (*26*). In contrast, smaller nanocrystals can behave similar to "super atoms" with highly quantized energy states (*27*). This may explain some of the trends we observe in terms

of the nature of the dynamic phenomena, but it is not clear from our results where the classical limit resides. What is clear, however, is that the smallest nanocrystals analyzed show the greatest degree of stability, whereas nanocrystals in the ~300 to 500 atoms size range are the most susceptible to nonlinear dynamic phenomena due to a strong correlation between dynamical surface effects and core coordination.

The average radial strain measures the relative deviation from perfect FCC crystallinity, and it is related to the crystallinity score. In those instances where the inverse proportionality between the two metrics is obvious (ESC5, $R = -0.85$, ESC3, $R = -0.98$, and ECT2, $R = -0.96$), the strain changes in a more concerted manner across the atoms of the nanocrystal (Fig. 3, A, D, and E), whereas in those instances that do not show any significant correlation, the strain changes in a less concerted manner at the atomic level (Fig. 3, B, C, and F). Mechanistically, a possible explanation for this phenomenon is that energy perturbations, either because of electron beam interactions or chemical changes, have long-ranging effects that influence the nanocrystal distinctly depending on its structural characteristics or the nature of the perturbation. This analysis also points to the respective power of the two metrics: Strain is mapped onto individual atoms and can be used for interpreting the structures at the atomic level, whereas the crystallinity score provides a scalar value based solely on the statistical analysis of the distributions of interatomic distances. The latter is useful for large-scale analysis of many structures to understand the crystalline properties of an ensemble of structures (Fig. 4), whereas strain provides information about lattice deformations at the atomic level (Fig. 3).

We analyze 15 distinct time trajectories to demonstrate the power of our methodology, but our computational approach can readily accommodate data processing at a much larger scale. It is now feasible, from a data analysis point of view, to analyze hundreds, if not thousands, of individual nanocrystal time trajectories. Furthermore, it is conceivable that atomic structure analysis algorithms for completely automated categorization of the nature of the structural dynamics could be developed in the future. Presently, the major limitation is the tedious experimental data collection. If this bottleneck could be overcome, then experiments could be designed that may shed light on the stochastic nature of small nanocrystals in solution and further advance our understanding of the basic physics governing colloidal nanoparticle assemblies.

MATERIALS AND METHODS

Synthesis of Pt nanocrystals

Pt nanocrystals of 2 to 3 nm in diameter were synthesized by mixing 0.05 mmol $(NH_4)_2Pt(II)Cl_4$ (99.995%, Sigma-Aldrich), 0.75 mmol of tetramethylammonium bromide (98%, Sigma-Aldrich), 1 mmol of polyvinylpyrrolidone (molecular weight of 29,000; Sigma-Aldrich), and 10 ml of ethylene glycol in a three-neck round bottom flask. We heated the mixture to 160°C and kept it at 160°C for 20 min. After cooling the solution to room temperature, we added 90 ml of acetone to precipitate the particles. The product was centrifuged at 4000 rpm for 5 min. We discarded the supernatant and redispersed the Pt nanocrystals redispersed in 5 mM Hepes buffer solution with pH 7.4.

Preparation of graphene liquid cells

We synthesized graphene on 25-μm-thick copper foil (99.8%, Alfa Aesar) by the chemical vapor deposition method. The copper foil in a quartz tube was heated to 1000°C for 30 min in hydrogen environment. Graphene was grown onto the copper foil with methane flows of 25 cm^3/min and hydrogen flows of 10 cm^3/min of at 1000°C. After 20 min, the product was rapidly cooled to room temperature with methane flow. Graphene TEM grids were prepared by transferring the graphene to a holey carbon grid using the direct transfer method. The graphene-covered copper foil was treated with weak oxygen plasma to etch the graphene on one side of the foil. A Quantifoil grid (Ted Pella) was placed onto the other grid side, on which graphene was not etched. Next, the copper foil substrate was etched with ammonium persulfate aqueous solution (0.1 g/ml). The graphene grid was washed with deionized water several times. The graphene liquid cell was fabricated with two graphene grids. A 0.5 μl of Pt nanocrystal solution was loaded onto a graphene grid. The other graphene grid was gently laid on the graphene grid with the liquid sample, so that the liquid sample was sandwiched between the two graphene sheets. The sealing of the liquid sample is accomplished through the strong interaction between the two graphene surfaces.

Acquisition of TEM images

TEM movies of Pt nanocrystals in the graphene liquid cell were obtained at a rate of 400 frames/s using TEAM I, an FEI Titan 80/300 TEM equipped with a postspecimen geometric- and chromatic-aberration corrector and a Gatan K2 IS direct electron detector. Thousands of images with 1920 × 1728 pixels and 0.358-Å pixel resolution were acquired at a dose rate of ~17 e−/pixel·frame or below at an acceleration voltage of 300 kV. The pixel size was confirmed on the basis of the known lattice spacing of the graphene sheets containing the nanocrystals. TEM images of rotating nanocrystals were used in the 3D reconstruction process. Successful 3D reconstruction of nanoparticles that differ in size, composition, and solvating molecules requires extensive optimization of imaging conditions, image processing, and reconstruction parameters. TEM imaging conditions must be optimized to obtain good signal-to-noise ratio of the 2D projected lattice for a given rotational rate, local thickness of the liquid, and image capture rate.

Denoising of the nanocrystal time trajectories through kernel-PCA

We previously used a deep autoencoding neural network architecture for denoising of one nanocrystal time trajectory before 3D reconstruction (*2*). The network was trained on the entire field of view, most of which consists of the graphene layers and liquid background. Neural network–based denoising of such a high-dimensional dataset is extremely challenging and requires careful selection of the appropriate network architecture in conjunction with an appropriate training algorithm run on a powerful distributed computer architecture. Here, we introduce much simpler and more cost-effective approach that outperforms the deep learning approach in terms of the quality of the atomic-resolution maps produced and the temporal resolution obtainable. Instead of operating on the entire field of view, we use our previously developed particle tracker (*7*) in conjunction with total variation-based denoising (*28*) to robustly extract nanocrystal time trajectories, consisting of windowed 2D views of one particle in different 3D orientations. Next, these one-particle time trajectories are denoised by nonlinear dimensionality reduction through generative kernel–principal components analysis (PCA) (*29*). Given a stack of noisy nanoparticle images $P_i, 1 \leq i \leq N_p$ we use kernel-PCA to produce a stack of denoised nanoparticles images $\widehat{P}_i, 1 \leq i \leq N_p$. The

kernel-PCA algorithm is implemented based on a pre-imaging learning algorithm (*30*, *31*) but uses the cosine similarity to derive the kernel and the corresponding optimization algorithm. The cosine similarity between two nanoparticle images P_i, P_j is defined as $K(P_i, P_j) = \frac{P_i \cdot P_j}{\|P_i\| \, \|P_j\|}$. The kernel-PCA method involves:

1) Computing the kernel K between all pairs of noisy nanoparticle images P_i, P_j.

2) Projecting each noisy nanoparticles image onto the kernel space to get the feature vectors.

3) Reducing the dimension of the kernel space using the standard singular value decomposition and a user-specified number of eigenvalues/eigenvectors to obtain feature vectors.

4) Back projecting the feature vectors with reduced dimensionality onto the image space to obtain the denoised nanoparticle images $\widehat{P}_i$.

The kernel-PCA approach has only one free parameter: The number of eigenvectors used for dimensionality reduction. Moreover, a robust numerical solution to the model training problem is available through the singular value decomposition and the pre-imaging algorithm (*30*, *31*). We used 500 kernel-PCA eigenvectors for all datasets analyzed here. We empirically determined this number to give optimal noise reduction while preserving high-resolution information. Training was done in parallel for up to 10 particle trajectories simultaneously on a standard workstation in less than an hour.

Periodic coupling of the unsupervised atomic model building to the iterative 3D orientation refinement

Instead of running hundreds of iterations of "classic" single-particle refinement (*11*, *13*, *14*), as we did in our previous studies (*5*–*7*), we now limit the number of iterations of 3D refinement to 10 before individual atomic densities are detected in the 3D reconstruction; spatial atomic coordinates derived; and a "clean" atomic density map, free from biasing background effects, is simulated and used to initialize another round of 3D refinement. These two phases of (i) classic single-particle 3D refinement and (ii) automated atomic model building and simulation of a "clean" 3D density for reinitialization are iterated until convergence, which is typically obtained in three to four rounds.

Atomic density threshold detection across nanocrystals of different sizes and with different degree of crystallinity

We previously published the method for unsupervised atomic model building (*17*), but a critical change that we had to make to enable reliable model building across nanocrystals of different sizes and with different degree of crystallinity was in how the threshold for atom detection is calculated. CNs are often used for atom peak thresholding (*5*, *32*). However, CN-based thresholding cannot be used in unsupervised approaches on its own because any procedure that would iteratively remove lowly coordinated atoms would eventually erode all the atomic positions. Therefore, we select T_{CN}, which is the CN bound that includes 95% of the detected atomic positions, as an initial CN threshold. Next, we subjected the 15% of atoms furthest from the center of mass of the nanocrystal to the following procedure. First, all atoms with CN $< T_{\mathrm{CN}} - 1$ are removed. Next, we iteratively remove all atoms with CN $< T_{\mathrm{CN}}$ and $R_{\mathrm{exp}} < R_{\mathrm{theoretical}}/2$, where R_{exp} is the experimentally measured atomic radius and $R_{\mathrm{theoretical}}$ is the theoretically derived atomic radius. This leads to a convergent thresholding procedure that is applicable across nanocrystals of different sizes and with different degree of crystallinity.

Adaptive nonuniform density map regularization based on ICMs

We introduce a method for nonuniform (local) regularization. Punjani *et al.* (*33*) put forward a general framework for optimization of the hyperparameters controlling the degree of smoothing introduced by regularization or filtering techniques. This nonuniform regularization approach, when coupled to the twofold cross-validated 3D refinement in CryoSPARC (*12*), provided adaptive regularization, thus addressing the issue that single-particle 3D refinement methods tend to simultaneously overfit and underfit datasets with large variations in local resolution due to flexibility or presence of disordered regions. This approach can be summarized as follows

1) Create low-pass–filtered representations of the even map using some uniform impulse-response function (cosine, Butterworth etc.).

2) Identify which filtered even map minimizes the Euclidean distance between each voxel and the corresponding voxel in the odd (raw) map.

3) Generate a nonuniformly filtered map by selecting the combination of optimally filtered voxels.

This approach recognizes that nonuniform regularization is inherently a real-space optimization problem, and it has proven to be superior to uniform regularization approaches in single-particle 3D refinement. Other nonuniform regularization approaches have also been developed for biomolecules that use deep neural networks in conjunction with prior structural information (*34*). Here, we introduce an alternative method for nonuniform volume regularization based on iterated conditional modes (ICMs) (*35*, *36*) for optimization of map connectivity in real space. A Gibbs random field describes the statistical properties of an interconnected network of non-negative items (set of voxels). We restrict the regularization to spatial neighborhood dependencies, i.e., voxel connectivity (the way in which pixels in 3D images relate to their neighbors). ICM is a deterministic algorithm for obtaining a configuration of a local maximum of the joint probability of a Gibbs random field by iteratively maximizing the probability of each variable (voxel) conditioned on the others in the neighborhood. We obtain a noise volume through subtraction of the even map from the odd map, followed by estimation of per-voxel noise SDs σ_i through voxel neighborhood analysis. We then apply ICM for nonuniform volume regularization of the even and odd maps independently in Algorithm 1 where $\lambda = 0.1$ is a regularization parameter. The discretization of the voxel values of the even and odd maps required for optimizing the local neighborhood quadratic potential is done through vector quantization.

Strain analysis

We define strain as the relative deformation of the structure compared to an ideal FCC lattice structure. The strain is calculated through differentiation of the displacement field (*37*). The displacement field is

ALGORITHM 1: Iterated Conditional Modes

Loop over iterations
  Loop over voxels x_i
    Identify n neighboring voxels y_j
    Maximize $p(\hat{x}_i) = \frac{(x_i - \hat{x}_i)^2}{2\sigma_i} + \lambda\left(\sum_{j=1}^{n} y_j^2 + n x_i^2 + 2 x_i \sum_{j=1}^{n} y_j\right)$
    Assign the gray level $\hat{x}_i \in [0,255]$ of the voxel accordingly
    Update the volume $x_i = \hat{x}_i$

Algorithm 1. Iterated Conditional Modes.

defined as the ideal atomic positions subtracted from the experimentally measured ones and interpolated using kernel density estimation (*38*). The relative atom positions a_i, b_i, and c_i are determined through lattice fitting. Let $r_{\mathrm{FCC},i}$ represent the ideal FCC atomic position of atom i; $r_{\mathrm{exp},i}$ its experimentally measured position, and e_i the residual of the fitting, then

$$r_{\mathrm{exp},i} = n_x a_i + n_y b_i + n_z c_i + e_i$$

$$r_{\mathrm{FCC},i} = n_x a_i^{(0)} + n_y b_i^{(0)} + n_z c_i^{(0)}$$

where $n_x, n_z, n_y \in \mathbb{Z}$ are normal vectors, $a_i^{(0)}, b_i^{(0)}, c_i^{(0)} \in \mathbb{R}$ are the unit cell vectors of bulk Pt, and the experimental unit cell vectors $a_i, b_i, c_i \in \mathbb{R}$ are determined through minimization of the sum of the square residuals. The displacement field u_i of atom i is evaluated as

$$u_i = r_{\mathrm{exp},i} - r_{\mathrm{FCC},i}$$

A Gaussian kernel is applied to generate a continuous function $u(r)$ of any vector position r

$$u(r) = \frac{\sum_i u_i \cdot \exp\left(-\frac{|r - r_{\mathrm{exp},i}|^2}{2\sigma^2}\right)}{\sum_i \exp\left(-\frac{|r - r_{\mathrm{exp},i}|^2}{2\sigma^2}\right)}$$

where $\sigma = 2$ Å is the SD of the Gaussian distribution, chosen based on leave-one-out cross-validation. The three displacement field components u_x, u_y, u_z are used to calculate the six 3D strain components

$$\epsilon_{xx} = \frac{\partial u_x}{\partial x}, \quad \epsilon_{xx} = \frac{\partial u_y}{\partial y}, \quad \epsilon_{zz} = \frac{\partial u_z}{\partial z}$$

$$\epsilon_{xy} = \frac{1}{2}\left(\frac{\partial u_x}{\partial y} + \frac{\partial u_y}{\partial x}\right), \quad \epsilon_{yz} = \frac{1}{2}\left(\frac{\partial u_y}{\partial z} + \frac{\partial u_z}{\partial y}\right),$$
$$\epsilon_{xz} = \frac{1}{2}\left(\frac{\partial u_x}{\partial z} + \frac{\partial u_z}{\partial x}\right)$$

ϵ_{xx}, ϵ_{yy}, and ϵ_{zz} represent compression or expansion of the lattice in the x, y, and z dimensions, respectively. ϵ_{xy}, ϵ_{yz}, and ϵ_{xz} represent deformations with angular components. We calculated the radial strain using a similar approach, with the radial displacement field, $u_i^{(r)}$, and radial strain component, ϵ_{rr}, described as

$$u_i^{(r)} = |\, r_{\mathrm{exp},i} - r_{\mathrm{c}} \,| - |\, r_{\mathrm{FCC},i} - r_{\mathrm{c}} \,|$$

$$\epsilon_{rr} = \frac{\partial u_{\mathrm{r}}}{\partial r}$$

Identification of a time-invariant core

We identified the atoms between the first temporal state and the second temporal state in the trajectory that had displacements smaller than half of the theoretical diameter of a platinum atom. Next, we averaged these "common" atomic positions and used them to identify common atoms in the third temporal states and so on. Once we had identified this time-invariant core, we went back through the temporal states in the trajectory and identified, for each state, the common atoms. This subset of common atoms of identical size across all temporal states is defined as the time-invariant core of atoms.

Crystallinity score

We calculated all pairwise atomic distances for the atomic structure of the particle of interest and compared that with distribution of pairwise atomic distances obtained from a simulated nanoparticle with ideal FCC lattice structure, spherically truncated to the same diameter. Next, the two distributions of atomic distances were compared using the Kolmogorov-Smirnov test (*39*) to calculate the probability that the null hypothesis was true, i.e., that the samples are drawn from the same reference distribution. We used this probability as a crystallinity score.

Parallel code implementation

The workflow implemented in the latest version of the software suite SINGLE (*7*) can be summarized as follows:

1) Particle tracking and time-trajectory extraction.
2) Time-trajectory denoising with kernel-PCA.
3) Time-restrained 2D analysis for image quality assessment.
4) Time-averaged 3D reconstruction and identification of trial time window boundaries.
5) Regularized 3D reconstruction in time windows.

We invested large efforts into serial central processing unit (CPU) code optimization and design of efficient parallel implementations for the various steps of the workflow. Steps 1 to 3 can be distributed across network connected computing units (sets of CPU cores) that work independently of each other on one time-trajectory each. This kind of parallelization scales linearly with the number of computing units. On a standard CPU workstation, steps 1 to 3 can be accomplished within a few hours. Steps 3 and 4 typically take 20 min to an hour on a standard CPU workstation, depending on the image size and the total number of images in the time trajectory. Steps 3 and 4 require some manual intervention for image quality assessment and trial time boundary selection, which typically involves less than half an hour of manual labor. Steps 4 and 5 have been optimized for shared-memory CPU architectures and are completed within a few hours using a handful of CPU cores (we typically use 12). We provide an implementation that generates individual scripts for each of the time trajectories that can be executed in a distributed computing environment using standard queue system software. While working on the 15 time trajectories used to generate the 66 atomic structures, there were many occasions where we needed to fix bugs or improve certain aspects of the 3D reconstruction code and rerun all the 3D reconstruction jobs. This was done at least 10 times in a timeframe of a few weeks without using any form of sophisticated distributed computing system. Hence, if equipped with a modern multicore CPU workstation, then it would be feasible to process hundreds of trajectories within a reasonable time frame. If running our codes on a distributed computing system, then this number could readily be scaled up by an order of magnitude. However, if such a large structure determination effort would be of interest to the community, it would be wise to invest some additional efforts into increased automation because steps 3 and 4 involve some manual intervention. Furthermore, the analysis of the reconstructed 3D density maps and their associated atomic coordinates would be cumbersome for so many structures, and increased automation would be necessary for efficient interpretation of maps and atomic coordinates.

Analyses of atomic structures

Visualization of 3D density maps and atomic coordinates were done in USCF Chimera (*40*). All quantitative structure analyses were done in the latest version of SINGLE (*7*).

Supplementary Materials

This PDF file includes:

Tables S1 and S2
Figs. S1 to S3

REFERENCES AND NOTES

1. X. Ye, M. R. Jones, L. B. Frechette, Q. Chen, A. S. Powers, P. Ercius, G. Dunn, G. M. Rotskoff, S. C. Nguyen, V. P. Adiga, A. Zettl, E. Rabani, P. L. Geissler, A. P. Alivisatos, Single-particle mapping of nonequilibrium nanocrystal transformations. *Science* **354**, 874–877 (2016).
2. S. Kang, J. Kim, S. Kim, H. Chun, J. Heo, C. F. Reboul, R. Meana-Pañeda, C. T. S. Van, H. Choi, Y. Lee, J. Rhee, M. Lee, D. Kang, B. H. Kim, T. Hyeon, B. Han, P. Ercius, W. C. Lee, H. Elmlund, J. Park, Time-resolved Brownian tomography of single nanocrystals in liquid during oxidative etching. *Nat. Commun.* **16**, 1158 (2025).
3. J. Lee, J. Yang, S. G. Kwon, T. Hyeon, Nonclassical nucleation and growth of inorganic nanoparticles. *Nat. Rev. Mater.* **1**, 16034 (2016).
4. K. C. Lai, Y. Han, P. Spurgeon, W. Y. Huang, P. A. Thiel, D. J. Liu, J. W. Evans, Reshaping, intermixing, and coarsening for metallic nanocrystals: Nonequilibrium statistical mechanical and coarse-grained modeling. *Chem. Rev.* **119**, 6670–6768 (2019).
5. B. H. Kim, J. Heo, S. Kim, C. F. Reboul, H. Chun, D. Kang, H. Bae, H. Hyun, J. Lim, H. Lee, B. Han, T. Hyeon, A. P. Alivisatos, P. Ercius, H. Elmlund, J. Park, Critical differences in 3D atomic structure of individual ligand-protected nanocrystals in solution. *Science* **368**, 60–67 (2020).
6. J. Park, H. Elmlund, P. Ercius, J. M. Yuk, D. T. Limmer, Q. Chen, K. Kim, S. H. Han, D. A. Weitz, A. Zettl, A. P. Alivisatos, 3D structure of individual nanocrystals in solution by electron microscopy. *Science* **349**, 290–295 (2015).
7. C. F. Reboul, J. Heo, C. Machello, S. Kiesewetter, B. H. Kim, S. Kim, D. Elmlund, P. Ercius, J. Park, H. Elmlund, SINGLE: Atomic-resolution structure identification of nanocrystals by graphene liquid cell EM. *Sci. Adv.* **7**, eabe6679 (2021).
8. D. Elmlund, H. Elmlund, Cryogenic electron microscopy and single-particle analysis. *Annu. Rev. Biochem.* **84**, 499–517 (2015).
9. A. Stewart, N. Grigorieff, Noise bias in the refinement of structures derived from single particles. *Ultramicroscopy* **102**, 67–84 (2004).
10. W. S. Tang, E. D. Zhong, S. M. Hanson, E. H. Thiede, P. Cossio, Conformational heterogeneity and probability distributions from single-particle cryo-electron microscopy. *Curr. Opin. Struct. Biol.* **81**, 102626 (2023).
11. S. H. Scheres, RELION: Implementation of a Bayesian approach to cryo-EM structure determination. *J. Struct. Biol.* **180**, 519–530 (2012).
12. A. Punjani, J. L. Rubinstein, D. J. Fleet, M. A. Brubaker, cryoSPARC: Algorithms for rapid unsupervised cryo-EM structure determination. *Nat. Methods* **14**, 290–296 (2017).
13. N. Grigorieff, FREALIGN: High-resolution refinement of single particle structures. *J. Struct. Biol.* **157**, 117–125 (2007).
14. C. F. Reboul, S. Kiesewetter, M. Eager, M. Belousoff, T. Cui, H. De Sterck, D. Elmlund, H. Elmlund, Rapid near-atomic resolution single-particle 3D reconstruction with SIMPLE. *J. Struct. Biol.* **204**, 172–181 (2018).
15. P. Ercius, M. Boese, T. Duden, U. Dahmen, Operation of TEAM I in a user environment at NCEM. *Microsc. Microanal.* **18**, 676–683 (2012).
16. H. P. Erickson, A. Klug, The Fourier transform of an electron micrograph: Effects of defocussing and aberrations, and implications for the use of underfocus contrast enhancement. *Ber. Bunsenges. Phys. Chem.* **74**, 1129–1137 (1970).
17. H. Wietfeldt, R. Meana-Paneda, C. Machello, C. F. Reboul, C. T. S. Van, S. Kim, J. Heo, B. H. Kim, S. Kang, P. Ercius, J. Park, H. Elmlund, Small, solubilized platinum nanocrystals consist of an ordered core surrounded by mobile surface atoms. *Commun. Chem.* **7**, 4 (2024).
18. P. Strasser, S. Koh, T. Anniyev, J. Greeley, K. More, C. Yu, Z. Liu, S. Kaya, D. Nordlund, H. Ogasawara, M. F. Toney, A. Nilsson, Lattice-strain control of the activity in dealloyed core-shell fuel cell catalysts. *Nat. Chem.* **2**, 454–460 (2010).
19. X. Huang, Z. Zhao, L. Cao, Y. Chen, E. Zhu, Z. Lin, M. Li, A. Yan, A. Zettl, Y. M. Wang, X. Duan, T. Mueller, Y. Huang, High-performance transition metal-doped Pt_3Ni octahedra for oxygen reduction reaction. *Science* **348**, 1230–1234 (2015).
20. M. Mavrikakis, B. Hammer, J. K. Norskov, Effect of strain on the reactivity of metal surfaces. *Phys. Rev. Lett.* **81**, 2819–2822 (1998).
21. P. D. Howes, R. Chandrawati, M. M. Stevens, Bionanotechnology., Colloidal nanoparticles as advanced biological sensors. *Science* **346**, 1247390 (2014).
22. M. Shao, A. Peles, K. Shoemaker, Electrocatalysis on platinum nanoparticles: Particle size effect on oxygen reduction reaction activity. *Nano Lett.* **11**, 3714–3719 (2011).
23. R. Reske, H. Mistry, F. Behafarid, B. Roldan Cuenya, P. Strasser, Particle size effects in the catalytic electroreduction of CO_2 on Cu nanoparticles. *J. Am. Chem. Soc.* **136**, 6978–6986 (2014).
24. G. Prieto, J. Zecevic, H. Friedrich, K. P. de Jong, P. E. de Jongh, Towards stable catalysts by controlling collective properties of supported metal nanoparticles. *Nat. Mater.* **12**, 34–39 (2013).
25. H. Zhang, T. Watanabe, M. Okumura, M. Haruta, N. Toshima, Catalytically highly active top gold atom on palladium nanocluster. *Nat. Mater.* **11**, 49–52 (2011).
26. N. Bohr, On the series spectra of elements. *Z. Phys.* **2**, 423–469 (1920).
27. P. Jena, Q. Sun, Super atomic clusters: Design rules and potential for building blocks of materials. *Chem. Rev.* **118**, 5755–5870 (2018).
28. L. I. Rudin, S. Osher, E. Fatemi, Nonlinear total variation based noise removal algorithms. *Phys. D: Nonlinear Phenom.* **60**, 259–268 (1992).
29. A. M. Jade, B. Srikanth, V. K. Jayaraman, B. D. Kulkarni, J. P. Jog, L. Priya, Feature extraction and denoising using kernel PCA. *Chem. Eng. Sci.* **58**, 4441–4448 (2003).
30. J. W. Gökhan H. Bakır, B. Schölkopf, in *Proceedings of the 17th International Conference on Neural Information Processing Systems (NIPS'03)* (MIT Press, 2003), pp. 449–456.
31. A. Cloninger, W. Czaja, T. Doster, The pre-image problem for Laplacian Eigenmaps utilizing L_1 regularization with applications to data fusion. *Inverse Problems* **33**, 074006 (2017).
32. S. Kim, J. Kwag, C. Machello, S. Kang, J. Heo, C. F. Reboul, D. Kang, S. Kang, S. Shim, S. J. Park, B. H. Kim, T. Hyeon, P. Ercius, H. Elmlund, J. Park, Correlating 3D surface atomic structure and catalytic activities of Pt nanocrystals. *Nano Lett.* **21**, 1175–1183 (2021).
33. A. Punjani, H. Zhang, D. J. Fleet, Non-uniform refinement: Adaptive regularization improves single-particle cryo-EM reconstruction. *Nat. Methods* **17**, 1214–1221 (2020).
34. B. Shi, K. Zhang, D. J. Fleet, R. A. McLeod, R. J. Dwayne Miller, J. Y. Howe, Deep generative priors for biomolecular 3D heterogeneous reconstruction from cryo-EM projections. *J. Struct. Biol.* **216**, 108073 (2024).
35. R. M. Taylor, Bayesian Compressive Sensing Using Iterated Conditional Modes. in *2011 IEEE International Workshop on Machine Learning for Signal Processing* (IEEE, 2011).
36. V. Pungpapong, M. Zhang, D. B. Zhang, Selecting massive variables using an iterated conditional modes/medians algorithm. *Electron. J. Stat.* **9**, 1243–1266 (2015).
37. M. J. Hytch, E. Snoeck, R. Kilaas, Quantitative measurement of displacement and strain fields from HREM micrographs. *Ultramicroscopy* **74**, 131–146 (1998).
38. R. Xu, C. C. Chen, L. Wu, M. C. Scott, W. Theis, C. Ophus, M. Bartels, Y. Yang, H. Ramezani-Dakhel, M. R. Sawaya, H. Heinz, L. D. Marks, P. Ercius, J. Miao, Three-dimensional coordinates of individual atoms in materials revealed by electron tomography. *Nat. Mater.* **14**, 1099–1103 (2015).
39. F. J. Massey, The Kolmogorov-Smirnov Test for Goodness of Fit. *J. Am. Stat. Assoc.* **46**, 68–78 (1951).
40. E. F. Pettersen, T. D. Goddard, C. C. Huang, G. S. Couch, D. M. Greenblatt, E. C. Meng, T. E. Ferrin, UCSF chimera - A visualization system for exploratory research and analysis. *J. Comput. Chem.* **25**, 1605–1612 (2004).

Acknowledgments

Funding: R.M.-P., C.J., C.T.S.V., C.F.R., and H.E. were supported by the Intramural Research Program of the NIH. C.J., W.C., and H.E. were supported by the NCI-UMD Partnership for Integrative Cancer Research. J.P. received support from the Samsung Science and Technology Foundation under project no. SSTF-BA2302-06. J.P. also received support from the Institute for Basic Science (IBS-R006-D1) and the National Research Foundation of Korea (NRF) grants funded by the Korean government (Ministry of Science and ICT) (nos. RS-2024- 00449965, RS-2024-00467226, and RS-2024-00421181). Experiments were performed at the Molecular Foundry, Lawrence Berkeley National Laboratory, which is supported by the US Department of Energy under contract no. DE-AC02-05CH11231. **Author contributions:** Conception/design of the work: P.E., W.C., J.P., and H.E. Software design: R.M.-P., C.J., C.T.S.V., C.F.R., and H.E. Data acquisition: P.E. All authors contributed to analysis/interpretation of data/results and writing of the manuscript. **Competing interests:** The authors declare that they have no competing interests. **Data and materials availability:** The 3D density maps and atomic coordinates supporting our findings are available at https://zenodo.org/records/15531575. The software that was used in this study is available at https://zenodo.org/records/15594642. All other data needed to evaluate the conclusions of the paper are present in the paper and/or the Supplementary Materials.

Submitted 10 April 2025
Accepted 11 July 2025
Published 6 August 2025
10.1126/sciadv.ady1413